Eurasian Journal of Physics and Functional Materials

2026, 10(2), 137-146

Synthesis and characterization of terbium-doped fluorine-substituted hydroxyapatite (HAp-F-Tb)

K.B. Zhangylyssov[1,*], S.Y. Pichkhidze[2], T.T. Alibay[1], G.B. Bairbayeva[1], A.S. Akhmetova[1], R.K. Daurenbekova[1], B.D. Kylyshbayev[1], A. Talgatuly[1], I. Mariyam[1], D.H. Daurenbekov[1]

[1]L.N. Gumilyov Eurasian National University. Astana. Kazakhstan

[2]Yuri Gagarin State Technical University of Saratov, Saratov, Russian Federation

E-mail: zh.keleshek@gmail.com

DOI: **10.32523/ejpfm.2026100203**
Received: 06.04.2026 - after revision

This work investigates the luminescent properties of fluorapatite doped with Tb^{3+} ions (HAp–F:Tb) to determine the nature of the luminescent centers and the excitation features. Biohydroxyapatite was obtained from cattle bone raw material by rapid pyrolysis followed by annealing at 750 °C ; doping was carried out by the solvation–precipitation method. The samples were characterized by X-ray diffraction analysis, IR spectroscopy, and photoluminescence spectroscopy in the 200–700 nm range. It was established that the main active center is Tb^{3+} : intense emission bands corresponding to the $^5D_4 \rightarrow {}^7F_5$, $^5D_4 \rightarrow {}^7F_4$, and $^5D_4 \rightarrow {}^7F_3$ transitions were recorded in the 490–620 nm region. The maximum intensity was observed under excitation at 220–260 nm and 355–377 nm, indicating direct excitation of Tb^{3+} and/or energy transfer from the matrix and defect levels. The obtained results demonstrate the promise of HAp–F-Tb as a luminescent material and the possibility of targeted modification of its optical properties through doping with rare-earth ions.

Keywords: Tb^{3+} ; photoluminescence; rare earth doping; biohydroxyapatite; luminescent centers; energy transfer; optical properties

Introduction

Apatite-based materials, primarily hydroxyapatite and fluorapatite, are of considerable interest in biomedicine and materials science due to their biocompatibility,

bioactivity, osteoconductivity, and ability to undergo extensive ionic substitutions within the crystal lattice [1]. Fluorapatite, as a stable calcium phosphate phase, can be obtained in nanocrystalline form and exhibits pronounced structural and luminescent properties when doped with rare-earth ions [2]. Theoretical calculations have shown that the substitution of calcium by rare-earth elements in the fluorapatite structure affects the unit-cell parameters, electronic structure, and surface chemical activity [3]. For the F/OH apatite system, it has also been established that variations in the fluorine-to-hydroxyl ratio are associated with the features of thermal expansion and thermodynamic behavior [4].

The promise of fluorapatite is further supported by the possibility of creating functional luminescent composites based on it, suitable for the sensitive detection of toxic ions in aqueous media [5]. The structural, thermal, and mechanical properties of apatite bioceramics can be purposefully modified through cationic and anionic substitutions, by introducing potassium and hydroxyl groups into the fluorapatite lattice [6]. Similarly, for terbium-doped hydroxyapatite, it has been shown that the heat-treatment regime significantly affects morphology, crystallinity, and luminescence intensity [7]. Replacing hydroxyapatite with fluorapatite in ceramic–polymer composites also lead to noticeable changes in specific surface area, porosity, particle size, and interfacial interactions [8].

Additional possibilities for controlling the properties of apatites are associated with co-doping, for example with magnesium and strontium, which makes it possible to obtain dense, homogeneous, and biocompatible fluorapatite materials stable in physiological media [9]. During the sintering of hydroxyapatite and fluorapatite mixtures, solid solutions may form, thereby expanding the possibilities for the targeted regulation of phase composition and structure [10]. For practical application in implantology, coatings based on substituted hydroxyapatite are of particular importance, including MgO/Tb,Eu-HAp systems, which demonstrate improved anticorrosive, antibacterial, and biological properties [11].

Of special interest are terbium-activated apatites due to the combination of luminescent characteristics and biocompatibility. It has been established that Tb^{3+}-doped hydroxyapatite is efficiently taken up by cells, is characterized by favorable tissue distribution, and does not cause pronounced toxicity, which is important for bioimaging applications [12]. In related biomedical studies, terbium compounds with phosphonate ligands have also demonstrated high affinity for hydroxyapatite and bone tissue, confirming the promise of this element for targeted bone-seeking systems [13]. In addition, terbium-containing luminescent nanosystems are used in analytical applications as sensitive fluorescent probes [14]. The high efficiency of Tb^{3+} as a luminescent center is also manifested in other crystalline matrices, where intense green emission and good scintillation characteristics are achieved [15]. In apatite-like phosphors, the co-introduction of terbium and samarium further enables tunable multicomponent luminescence [16].

It has been shown for hydroxyapatite that Tb^{3+} can be incorporated into the structure within certain concentration limits, causing changes in the morphology, structure, and optical properties of the material [17]. A promising direction is also represented by Tb^{3+}-doped citrate-functionalized carbonate

apatite nanoparticles, which are suitable for intracellular imaging without the use of additional dyes [18]. Along with terbium, other rare-earth ions can also be successfully incorporated into the hydroxyapatite structure: for example, gadolinium enhances the luminescent, electrical, and thermal characteristics [19], while neodymium provides near-infrared emission, which is of interest for optical biomedical technologies [20].

In this work, terbium-doped fluorine-substituted hydroxyapatite was synthesized, and its structural, morphological, elemental, and luminescent properties were studied using XRD, FTIR, SEM-EDX, and electronic property measurements.

Materials and Methods

Biohydroxyapatite was obtained from biological raw material (bovine bones) by the method of fast pyrolysis. During this procedure, the bones were first defatted in boiling water for 4–6 hours. The obtained bones were divided into fragments 3–8 mm thick and dried in ovens at about $200\,^{\circ}\mathrm{C}$. Fast pyrolysis was carried out using thermal treatment of a certain amount (300 g) of 5 prepared bone fragments at a temperature of $(750 \pm 10)\,^{\circ}\mathrm{C}$ in a preheated muffle furnace [21]. The treatment duration was 30 min. This procedure ensured the thermal decomposition of the organic components of the bone into a gaseous state and the removal of pyrolysis gas. It was previously established that only at a pyrolysis temperature of $600\,^{\circ}\mathrm{C}$ and below did the obtained samples contain a residual fraction of bioorganic components (approximately 4 wt.%). The obtained product was ground in a mortar for several hours.

For fluorine incorporation, 10 grams of the obtained pure hydroxyapatite were used. First, a solution was prepared by dissolving 1 gram of NaF powder in 100 ml of deionized water. The obtained solution was mixed with the powder until a suspension was obtained and stirred for several hours, after which the liquid phase was separated by centrifugation. The obtained precipitate was repeatedly washed with distilled water and dried at 80–110 $^{\circ}$C.

A similar method was used for the incorporation of fluorinated hydroxyapatite. $\mathrm{Tb(NO_3)_3 \cdot 5H_2O}$ was also dissolved in distilled water and mixed with fluorinated hydroxyapatite. To prevent dissolution, the pH level was maintained in the range of $\mathrm{pH} = 8$–9. After drying and washing the solution, the obtained sample was annealed in a muffle furnace at $550\,^{\circ}\mathrm{C}$ for several hours.

To study the luminescent properties, the powders were pressed into copper holders with a thickness of 0.5 mm and a diameter of about 10 mm. Pressing was carried out using a manual press at a pressure of approximately 0.1–0.2 MPa.

The obtained samples were analyzed by photoluminescence, IR spectroscopy, X-ray diffraction, and scanning electron microscopy with an EDS detector. Luminescence characteristics were recorded in the spectral range of 200–700 nm using a Solar CM 2203 spectrofluorimeter (Solar, Belarus). The molecular structure was studied in the range of 400–4000 cm^{-1} using a Jasco IR-4700 infrared spectrometer (Japan) equipped with an ATR module. Structural and phase analysis was carried out on a Bruker D6 Phaser diffractometer (Germany) in the angular range

of $2\theta = 20-80^\circ$. A Hitachi TM4000plusII scanning electron microscope with a Bruker EDS detector (Japan) was used.

Results and discussion

Structural, morphological, and elemental analysis of the samples

To determine the phase composition of the investigated samples, X-ray diffraction analysis (XRD) was carried out. Figure 1 shows the X-ray diffraction patterns of pure hydroxyapatite obtained from biological raw material (HAp), fluorine-substituted hydroxyapatite (HAp-F), and terbium-doped fluorine-substituted hydroxyapatite in the angular range of 2θ from 20° to 80°. All measured samples have a hexagonal crystal lattice (space group $P6_3/m$), according to the positions of the diffraction peaks and PDF card 15-0876.

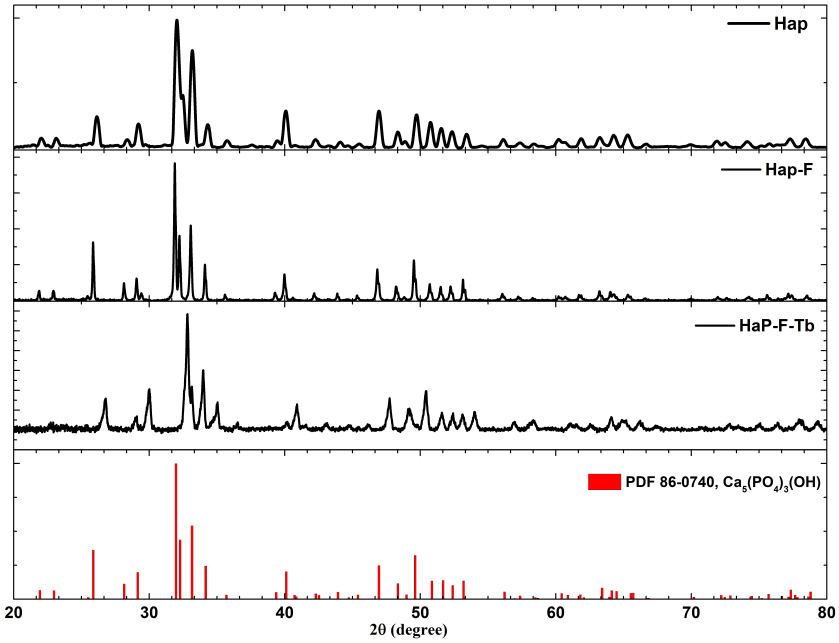

Figure 1. X-ray diffraction analysis of the pure HAp, HAp-F and HAp-F-Tb samples.

The change in the interplanar spacing d was calculated using Bragg's law (Table 1):

$$d = \frac{\lambda}{2\sin\theta} \tag{1}$$

where $\lambda = 1.5406$ Å, $\theta = 2\theta/2$.

A slight broadening of some peaks and a decrease in their intensity are observed. It can be seen that after fluorine incorporation, the interplanar spacing increases on average by 0.59%. When terbium dopant is added to the fluorine-substituted hydroxyapatite sample, the interplanar spacing decreases on average by 2%, while for some peaks it increases by 0.6%.

Such non-uniform changes in the interplanar spacings are associated with the hexagonal structure ($a = b \neq c$) and with partial destabilization of the crystal lattice caused by the incorporation of rare-earth Tb^{3+} ions, whose ionic radius differs from that of Ca^{2+}. Such substitutions can cause local distortions in the structure, reducing the degree of crystallinity and increasing the defectiveness of the material.

This is confirmed by the calculation of the degree of crystallinity ($X_c = (S_{cr} + S_{am})/S_{cr} * 100\%$) for the main materials HAp-F and HAp-F-Tb. It was found that the HAp-F sample has a crystallinity degree of 89.1%, while the HAp-F-Tb sample has a crystallinity degree of 87.9%. No additional phases or impurities were detected in the X-ray diffraction spectra, indicating the successful incorporation of fluorine and terbium into the hydroxyapatite lattice without the formation of secondary compounds. This also confirms the high chemical compatibility of these ions with the $Ca_5(PO_4)_3(OH)$ matrix.

Table 1.
Changes in interplanar spacing of HAp, HAp-F and HAp-F-Tb samples calculated from XRD data.

No. peak	PDF		HAp		HAp-F		HAp-F-Tb	
	2θ	d, Å	$\Delta 2\theta$	Δd, %	$\Delta 2\theta$	Δd, %	$\Delta 2\theta$	Δd, %
1	31.96	2.798	0.07	−0.22%	−0.07	0.22%	0.85	−2.52%
3	34.15	2.623	0.18	−0.52%	−0.05	0.15%	−0.17	0.49%
4	40.1	2.247	−0.03	0.08%	−0.14	0.36%	0.88	−2.06%
5	46.94	1.934	0.01	−0.02%	−0.12	0.24%	0.79	−1.56%
6	50.86	1.794	−1.13	2.17%	−1.34	2.58%	−0.44	0.81%

Thus, X-ray diffraction analysis showed that Tb^{3+} - and fluorine-doped hydroxyapatite preserves the hexagonal structure of fluorapatite, which makes these materials promising for further studies in luminescent and biomedical applications. The results of infrared spectroscopy (Figure 2) confirm the formation of the apatite structure and allow a more detailed study of the effect of doping on the local structure. For comparison with the main sample, vibrations in the infrared region were measured for pure biohydroxyapatite and fluorine-substituted hydroxyapatite, together with the main investigated HAp-F-Tb sample.

For the Tb^{3+} -containing sample (Figure 2), the main bands characteristic of phosphate ions are preserved, in particular the intense maxima at 1097 cm^{-1}, 1041 cm^{-1}, and 960 cm^{-1}, corresponding to ν_3 PO_4^{3-}, as well as deformation vibrations at 604 cm^{-1}, 574 cm^{-1}, and 472 cm^{-1}, corresponding to ν_4 PO_4^{3-}. At the same time, slight band shifts are observed compared with pure hydroxyapatite at 1037 and 601 cm^{-1}, especially in the region of symmetric and deformation vibrations, which may indicate a change in the local chemical environment of PO_4^{3-} due to the incorporation of rare-earth ions into the crystal lattice.

In addition, in the doped sample, the intensity of the bands associated with the presence of hydroxyl groups noticeably decreases, indicating the substitution of OH^- at 630 cm^{-1} by F^- during Tb incorporation. The absence of the main OH band is associated with the biological origin of hydroxyapatite and the appearance of carbonate groups at 2500 and 2500 cm^{-1}.

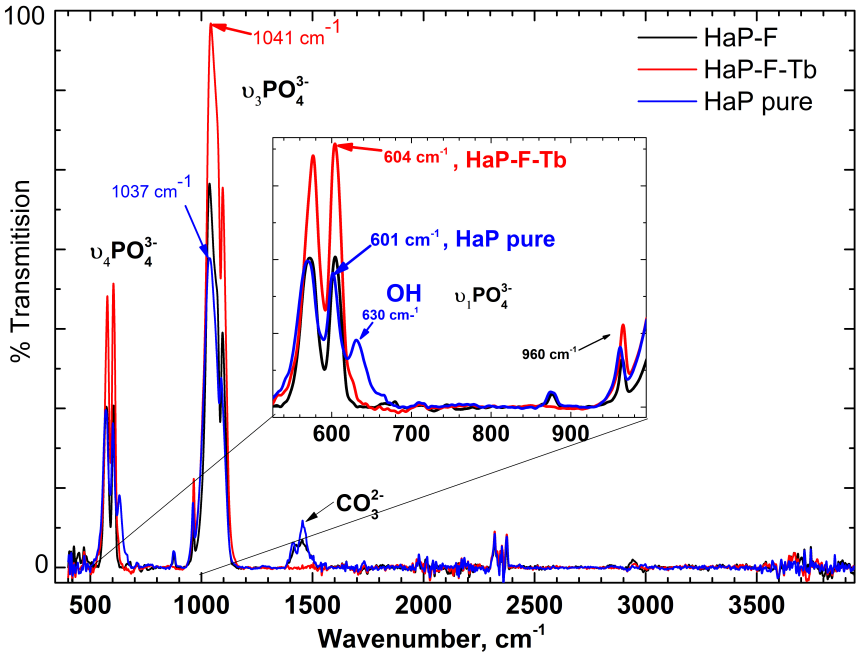

Figure 2. IR spectrum of the pure HAp, HAp-F and HAp-F-Tb.

Thus, the IR analysis results show that the incorporation of Tb^{3+} ions into the hydroxyapatite structure occurs without destruction of the apatite matrix and is accompanied by characteristic changes in the vibrational spectrum.

The study of the morphological characteristics and elemental analysis of the investigated HAp–F-Tb sample confirms the data obtained from X-ray structural analysis and vibrational spectroscopy. As shown in Figure 3, the obtained sample has a powder-like morphology with an average grain size of 1–2 μm. The powders form agglomerates with sizes of up to 200 μm.

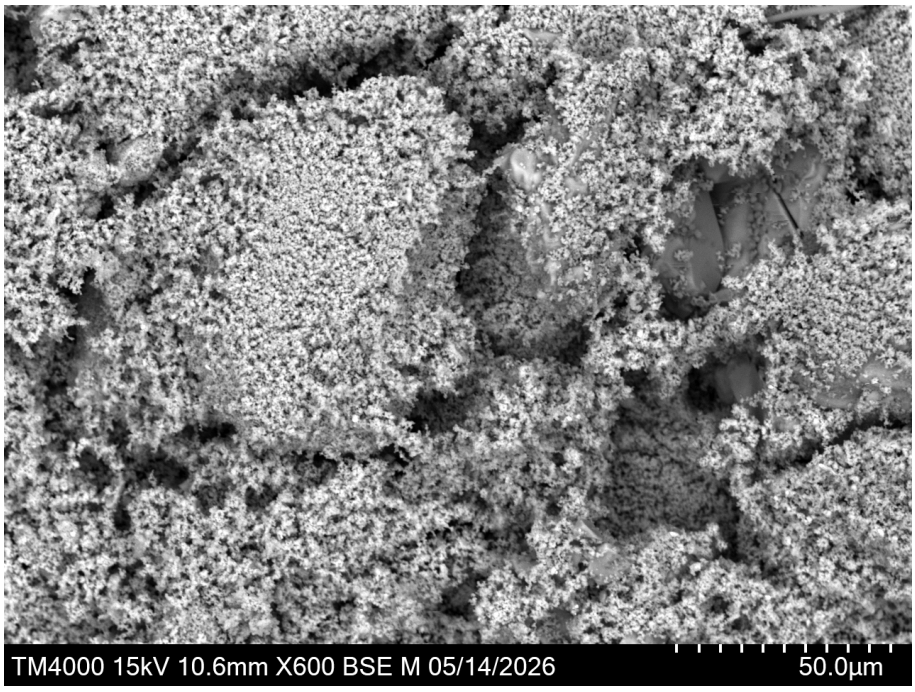

Figure 3. SEM images of the HAp–F-Tb

The measurement of the chemical element distribution by mapping (Figure 4, left) shows the average distribution of the main particles of the base material and the impurities of fluorine and terbium. Figure 4, right, shows the elemental analysis in a 50 µm region.

It can be seen that all spectral lines of the main chemical elements of the HAp–F-Tb sample are present. The table of mass fractions provides an approximate estimation of the incorporated fluorine impurities (2.95%) and terbium impurities (4.17%). Due to the local nature of EDS spectral measurements, differences from other measured regions are possible.

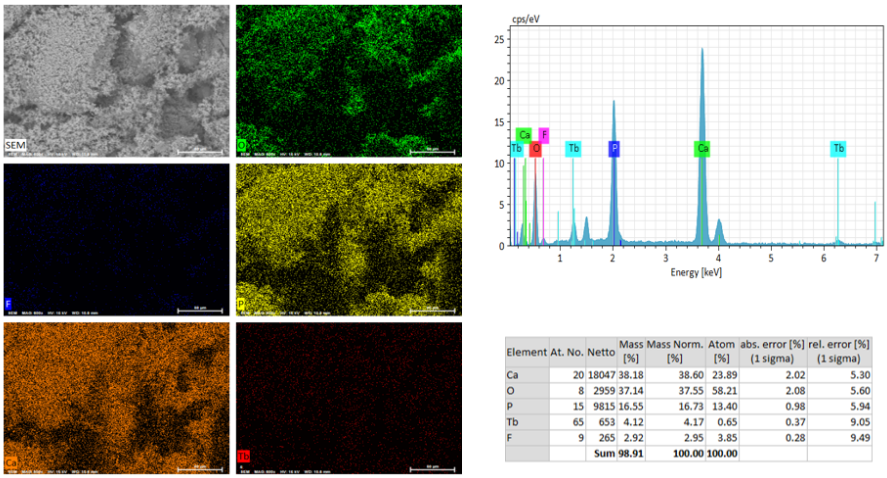

Element	At. No.	Netto	Mass [%]	Mass Norm. [%]	Atom [%]	abs. error [%] (1 sigma)	rel. error [%] (1 sigma)
Ca	20	18047	38.18	38.60	23.89	2.02	5.30
O	8	2959	37.14	37.55	58.21	2.08	5.60
P	15	9815	16.55	16.73	13.40	0.98	5.94
Tb	65	653	4.12	4.17	0.65	0.37	9.05
F	9	265	2.92	2.95	3.85	0.28	9.49
		Sum	**98.91**	**100.00**	**100.00**		

Figure 4. SEM–EDX elemental mapping and spectrum/scanning analysis of the HAp–F-Tb.

Luminescence properties of Tb-doped fluorine-substituted hydroxyapatite

To study the optical properties of terbium-doped fluorine-substituted hydroxyapatite, photoluminescence and excitation spectra were recorded at various wavelengths. The obtained data made it possible to determine the nature of the luminescent centers, the excitation pathways, and the influence of rare-earth ions on the energy-level structure.

In the emission spectra under excitation at 220 and 250 nm (Figure 5a), intense bands are observed in the green and yellow-orange regions of the spectrum, with maxima near 490, 545, 585, and 620 nm. The main peak at 545 nm corresponds to the $^5D_4 \rightarrow {}^7F_5$ transition of the Tb^{3+} ion. The $^5D_4 \rightarrow {}^7F_4$ and $^5D_4 \rightarrow {}^7F_3$ transitions produce bands at 585 and 620 nm, respectively, indicating the effective incorporation of Tb^{3+} into the lattice and the formation of stable emission centers. Under excitation at wavelengths of 400, 418, 485, and 533 nm (Figure 5b), the same spectral profile is retained; however, the intensity decreases, especially at 533 nm, which indicates the lower efficiency of direct terbium excitation in this region.

A change in the excitation wavelength from 318 to 377 nm (Figure 6a) demonstrates that the emission maximum remains at 545 nm, while the intensity depends on the excitation wavelength: it reaches a maximum at 355 and 377 nm,

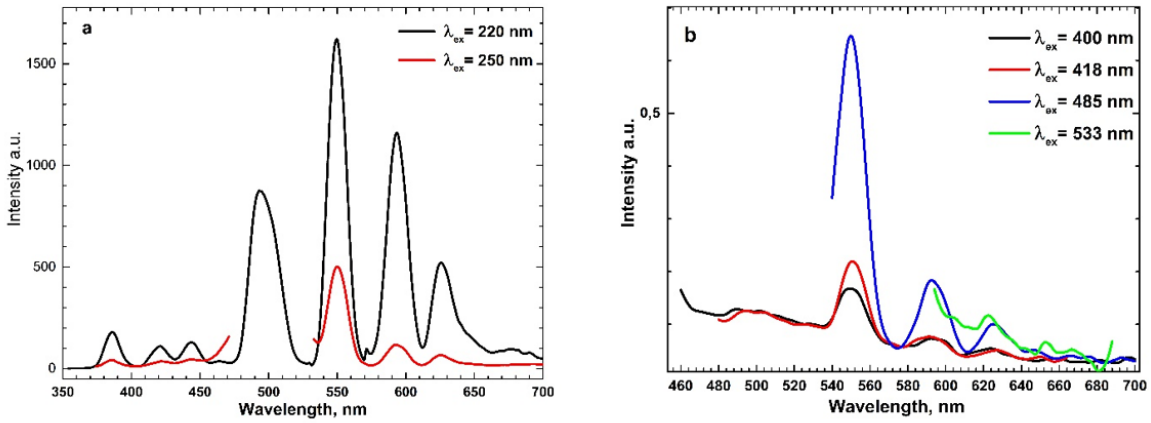

Figure 5. Emission spectra under excitation at (a) 220 nm and 250 nm, and (b) 400 nm, 418 nm, 485 nm, and 533 nm for the HAp-F-Tb

which may be associated with resonant energy transfer from the host material to Tb^{3+} dopant ions. This is also confirmed by the excitation spectra recorded at emission wavelengths of 385 and 420 nm (Figure 6b), where broad bands are observed in the UV region (220–250 nm), as well as shoulders in the 270–320 nm range, reflecting the contribution of the phosphate matrix and cationic defects.

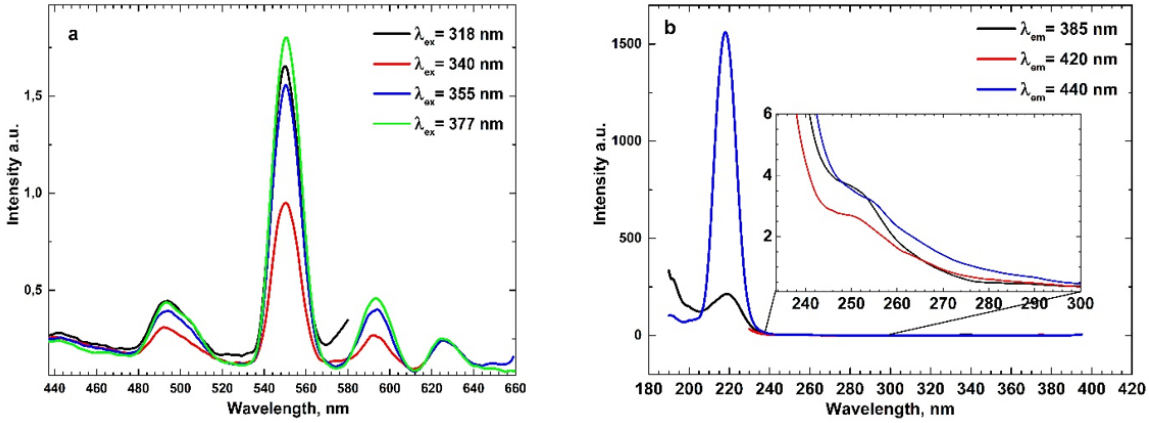

Figure 6. (a) Emission spectra under excitation at 318 nm, 340 nm, 355 nm, and 377 nm and (b) excitation spectra for the emission bands at 385 nm and 420 nm for the HAp-F-Tb

In the excitation spectra recorded at emission wavelengths of 494 nm, 504 nm, and 548 nm (Figure 7a), excitation bands are observed both in the UV region and in the visible range, around 330–420 nm. The latter can be interpreted as intra-configurational transitions of the Tb^{3+} ion between the $^5G_6$, $^5D_3$, and $^5D_4$ levels. This interpretation is supported by the coincidence of the excitation and emission maxima, especially at 494 and 504 nm, which indicates the possibility of self-luminescence. In the excitation spectra at longer-wavelength emission bands (594, 600, and 625 nm; Figure 7b), the UV bands are retained, but their intensity decreases, which corresponds to the lower probability of the respective transitions $^5D_4 \rightarrow {}^7F_3$, $^7F_2$ and a lower quantum yield.

Thus, the spectroscopic analysis results show that Tb^{3+} is the luminescent center ($^5D_4 \rightarrow {}^7F_3$) in the HAp-F-Tb system. Its characteristic transitions are reproducible at different excitation wavelengths, while the maximum excitation

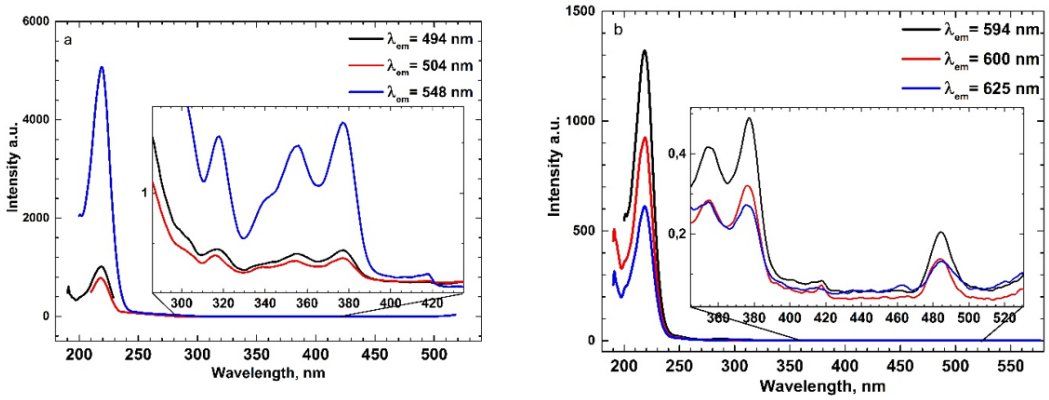

Figure 7. Excitation spectra for the emission bands at (a) 494 nm, 504 nm, and 548 nm and (b) 594 nm, 600 nm, and 625 nm for the HAp-F-Tb sample.

efficiency is achieved in the 220–260 nm region and at 355–377 nm.

Conclusion

The optical properties of HAp-F-Tb were investigated to determine the nature of the luminescent centers and the features of the excitation processes. The analysis of the photoluminescence and excitation spectra at different wavelengths made it possible to characterize in detail the emitting transitions, as well as the influence of the matrix structure on the luminescence efficiency.

It was established that the Tb^{3+} ion is the main active luminescent center in the studied system. Its characteristic transitions, in particular $^5D_4 \rightarrow {}^7F_5$, $^5D_4 \rightarrow {}^7F_4$, and $^5D_4 \rightarrow {}^7F_3$, give rise to intense bands in the green and yellow-orange regions of the spectrum, with maxima in the 490–620 nm range. The highest luminescence intensity is achieved under excitation in the 220–260 nm region, as well as at 355–377 nm, indicating the possibility of efficient excitation of Tb^{3+} both directly and through resonant energy transfer from the host lattice or defect levels.

The analysis of the excitation spectra showed the presence of broad bands in the UV range and additional shoulders in the 270–420 nm region, which is associated with the contribution of the phosphate matrix and cation vacancies. Intra-configurational transitions in the Tb^{3+} ion were also detected, as confirmed by characteristic maxima in the 330–420 nm region.

Thus, the obtained results demonstrate the promise of Tb^{3+}-doped fluorine-substituted hydroxyapatite as an efficient luminescent material, with the possibility of further modifying its properties through the introduction of other rare-earth elements and the control of structural parameters. This work lays the foundation for further research in the field of functional materials for photonics and optoelectronics.

Acknowledgments

This research was funded by the Science Committee of the Ministry of Science and Higher Education of the Republic of Kazakhstan (Grant No. AP22788773)

References

[1] I.A. Neacsu et al., Nanomaterials **9** (2019) 239. [*CrossRef*]
[2] P. Singh, I.M. Nagpure, Applied Surface Science **681** (2025) 161587. [*CrossRef*]
[3] X. Wang et al., Minerals **9** (2019) 500. [*CrossRef*]
[4] G.L. Hovis et al., American Mineralogist **99** (2014) 2171–2175. [*CrossRef*]
[5] H. Liu et al., Environmental Science: Nano **8** (2021) 3711–3721. [*CrossRef*]
[6] J.B. Slimen et al., Coatings **11** (2021) 858. [*CrossRef*]
[7] H. Yin, Y. Li, J. Bai, M. Ma, J. Liu, Journal of Materiomics **3** (2017) 144–149. [*CrossRef*]
[8] L. Borkowski, K. Palka, L. Pajchel, Materials **18** (2025) 4538. [*CrossRef*]
[9] M.H. Ghaemi et al., Processing and Application of Ceramics **16** (2022) 218–229. [*CrossRef*]
[10] X. Li, Q. Zou, W. Li, H. Chen, Scientific Reports **8** (2018) 11267. [*CrossRef*]
[11] S. Sathishkumar et al., Journal of Science: Advanced Materials and Devices **5** (2020) 545–553. [*CrossRef*]
[12] Y. Wei, Y. He, X. Li, H. Chen, X. Deng, Molecules **22** (2017) 1043. [*CrossRef*]
[13] P. Sitarica et al., International Journal of Molecular Sciences **26** (2025) 10392. [*CrossRef*]
[14] A. Serag et al., RSC Advances **15** (2025) 19468–19479. [*CrossRef*]
[15] A. Baillard et al., RSC Advances **15** (2025) 18802–18813. [*CrossRef*]
[16] K. Nie et al., Heliyon **8** (2022) e12566. [*CrossRef*]
[17] A.V. Paduraru et al., Nanomaterials **11** (2021) 2442. [*CrossRef*]
[18] J. Gomez-Morales et al., Nanomaterials **12** (2022) 1257. [*CrossRef*]
[19] B. Demirel, E. Saban, A. Yaras, F. Akkurt, Journal of Asian Ceramic Societies **9** (2021) 865–873. [*CrossRef*]
[20] K. Gayathri, G.A. Kumar, S.I.R. Manrique, C. Santhosh, D.K. Sardar, Journal of Luminescence **185** (2017) 180–186. [*CrossRef*]
[21] D.A. Zimnyakov et al., Ceramics **8** (2025) 36. [*CrossRef*]